

SHeRLoc: Synchronized Heterogeneous Radar Place Recognition for Cross-Modal Localization

Hanjun Kim¹, Minwoo Jung², Wooseong Yang² and Ayoung Kim^{2*}

Abstract—Despite the growing adoption of radar in robotics, the majority of research has been confined to homogeneous sensor types, overlooking the integration and cross-modality challenges inherent in heterogeneous radar technologies. This leads to significant difficulties in generalizing across diverse radar data types, with modality-aware approaches that could leverage the complementary strengths of heterogeneous radar remaining unexplored. To bridge these gaps, we propose SHeRLoc, the first deep network tailored for heterogeneous radar, which utilizes RCS polar matching to align multimodal radar data. Our hierarchical optimal transport-based feature aggregation method generates rotationally robust multi-scale descriptors. By employing FFT-similarity-based data mining and adaptive margin-based triplet loss, SHeRLoc enables FOV-aware metric learning. SHeRLoc achieves an order of magnitude improvement in heterogeneous radar place recognition, increasing recall@1 from below 0.1 to 0.9 on a public dataset and outperforming state-of-the-art methods. Also applicable to LiDAR, SHeRLoc paves the way for cross-modal place recognition and heterogeneous sensor SLAM. The source code will be available upon acceptance.

Index Terms—Localization, SLAM, Range Sensing

I. INTRODUCTION

PLACE recognition (PR) is a cornerstone of robust localization in autonomous driving, enabling vehicles to identify previously visited locations. Traditionally, cameras and LiDAR have dominated PR due to their rich data representations [1, 2]. However, their susceptibility to adverse conditions has shifted attention to radar, which offers unparalleled robustness by penetrating fog, rain, snow, and dust [3, 4]. Early radar-based PR mostly leveraged 360° spinning radars, establishing a foundation for robust localization [5–10]. Building on this foundation, compact and cost-effective system-on-a-chip (SoC) radars have been integrated into PR tasks [11–13]. More recently, modern 4D radars, capable of capturing range, azimuth, elevation, and radial velocity, have also been adopted in radar-based PR [14, 15].

Despite the growing adoption of radar in robotics, the majority of research has been confined to homogeneous sensor systems, overlooking the integration and cross-modality challenges inherent in heterogeneous radar technologies. Notably, different radar systems operate under distinct sensing principles, leading to substantial variations in noise characteristics,

This work has been submitted to the IEEE for possible publication. Copyright may be transferred without notice, after which this version may no longer be accessible.

¹H. Kim is with the Dept. of Future Automotive Mobility, SNU, Seoul, S. Korea hanjun815@snu.ac.kr

²M. Jung, W. Yang and A. Kim are with the Dept. of Mechanical Engineering, SNU, Seoul, S. Korea [moonshot, yellowish, ayoungk]@snu.ac.kr

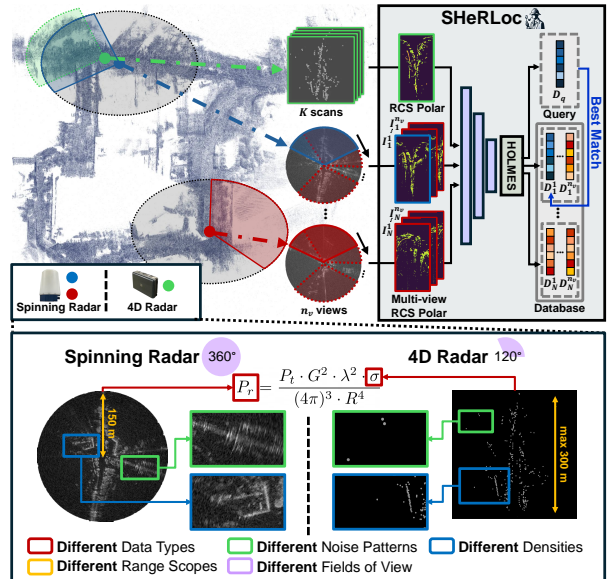


Fig. 1: SHeRLoc addresses the modality gap between heterogeneous radar systems through the proposed RCS polar matching.

point density, measurement range, and field of view (FOV). As a result, methods designed for homogeneous radar systems fail to generalize across diverse radar configurations. Moreover, radar types are suited for different tasks: spinning radar, with its dense 360° measurements, is ideal for building comprehensive mapping databases, while 4D radar, more prevalent in modern vehicles, excels in real-time dynamic sensing and is well-suited for query generation under resource constraints. Despite these complementary properties, existing radar-based PR approaches do not account for the differences between radar modalities, leaving the problem of heterogeneous radar PR largely unresolved. These challenges highlight the need for a new approach: *modality-aware heterogeneous radar PR*.

In this paper, we propose SHeRLoc, Synchronized Heterogeneous Radar Place Recognition for Cross-Modal Localization. Despite the inherent challenges of heterogeneous radars, as illustrated in Fig. 1, SHeRLoc enables radar-agnostic learning by leveraging novel Radar Cross Section (RCS) polar bird’s-eye view (BEV) synchronization and multi-view generation. Additionally, we present HOLMES, a feature aggregation network that addresses radar speckle noise and multipath issues through a learnable weight matrix and ghostbin, while ensuring stable optimal transport with an adaptive entropy-regularized Sinkhorn algorithm. Unlike existing methods that rely on high-dimensional single-scale descriptors [1, 16], which may lack global scene context, HOLMES integrates both local RCS patterns and global structural information into

a compact, multi-scale descriptor. Our FOV-aware data mining enables spatially and viewpoint-aware metric learning, while the adaptive margin-based triplet loss directs the model to focus on harder negative samples. SHeRLoc achieves rotation invariance by integrating the translation-equivariance of multi-view generation with the translation-invariance of HOLMES in the polar domain. By overcoming sparsity and noise patterns, SHeRLoc addresses the kidnapped robot problem with 4D radar on a spinning radar map, while also being applicable to Frequency modulated continuous wave (FMCW) LiDAR.

Our contributions can be summarized as follows:

- We present SHeRLoc, a deep network designed to tackle the complexities of heterogeneous radars, including sparsity, diverse FOV, and varying data dimensions. To the best of our knowledge, this is the first approach specifically designed for heterogeneous radar systems.
- To address variations in data type, density, and FOV, we propose an optimization-based RCS matching and multi-view polar projection, enabling radar-agnostic learning. Our novel preprocessing pipeline effectively removes dynamic objects, clutter, and ground return.
- We propose a hierarchical optimal transport-based feature aggregation method for rotationally robust descriptors, overcoming the loss of global context in traditional high-dimensional descriptors. Our FFT-similarity-based data mining and adaptive margin-based triplet loss ensure spatially and viewpoint-aware metric learning.
- We evaluate SHeRLoc against state-of-the-art (SOTA) methods under diverse scenarios (homogeneous, heterogeneous, single-/multi-session, and lidar-to-radar) and demonstrate superior performance in extreme conditions (e.g., crowded, snow, and random rotation). We open-source the code for the radar robotics community.

II. RELATED WORK

A. Radar Place Recognition

Spinning radar and SoC radar are the two primary sensor types studied in radar-based PR. Early radar-based PR mainly utilized spinning radar, leveraging their 360° FOV and relatively dense representations. To achieve rotation invariance, Radar Scan Context [4] extended the LiDAR-based Scan Context [2], while Kidnapped Radar [6] introduced a NetVLAD-based learning approach. As time efficiency became critical, RaPlace [8] and FFTRadVLAD [9] adopted the Fourier Transform, and ReFeree [10] proposed a compact one-dimensional descriptor. These advancements established a foundation for radar-based PR but faced challenges when the sensor output is sparse point data, as seen in SoC radar.

The adoption of SoC radars in PR tasks has rendered traditional spinning radar-based methods less applicable due to the narrower FOV and sparser data of SoC radars, necessitating new approaches. Notably, AutoPlace [11] increased the FOV by using five automotive radars and overcame sparsity by utilizing a spatial-temporal encoder. However, it relies on high-dimensional descriptors and requires an additional reranking process. mmPlace [12] expands the FOV by leveraging a rotating platform and concatenating heatmaps, while SPR [13]

proposes a lightweight method using a single radar scan. However, both methods are vulnerable in dynamic environments as they do not incorporate velocity information. More recently, TransLoc4D [14] employs transformer architectures to integrate geometry, intensity, and velocity from 4D radar, but remains susceptible to rotation due to its reliance on a single viewpoint. Hilger et al. [15] proposed a pipeline incorporating both similar and opposing viewpoints; nevertheless, this approach is still limited to just two viewpoints, and the challenge of PR across heterogeneous radar with distinct FOV and varying data characteristics remains unsolved.

B. Challenges in Heterogeneous Sensor Place Recognition

Heterogeneous sensor PR requires seamless integration of sensors with diverse FOVs and distinct data characteristics. Radar-to-LiDAR [17] and RaLF [18] introduced cross-modal PR methods that retrieve query spinning radar scans from existing LiDAR maps. However, these methods are limited in addressing different FOVs. Cattaneo et al. [19] proposed a LiDAR-Camera PR model using global descriptors, but it also overlooks the variations in FOV. Specifically, 360° point clouds tend to include irrelevant scene information outside the FOV of RGB images. ModaLink [20] attempted to mitigate this by using camera pose priors to crop point clouds, but this cropping approach is impractical. In response, LCPR [21] and CRPlace [22] proposed sensor fusion-based methods that integrate data using panoramic views or BEV, while Yao et al. [16] introduced a multi-view xNetVLAD that accounts for FOV differences. However, these methods require separate networks for each modality. Recently, HeLiOS [23] introduced overlap-based learning with guided-triplet loss for heterogeneous LiDAR PR, though it is limited by LiDAR's high point density and minimal differences between heterogeneous LiDAR scans. In contrast to previous methods, we propose a novel RCS polar matching that efficiently integrates diverse FOV and data dimensions to achieve sensor-agnostic learning, overcoming radar's sparsity and distinct noise patterns.

III. METHODS

As illustrated in Fig. 2, SHeRLoc transforms 4D radar scan $\mathcal{S}_{4D} \in \mathbb{R}^{N \times 5}$, with N points, and spinning radar scan $\mathcal{S}_{\text{spin}} \in \mathbb{R}^{N_r \times N_a}$, with N_r range bins and N_a azimuth bins, into RCS polar BEV images denoted as $I_{4D}, I_{\text{spin}} \in \mathbb{R}^{H \times W}$. Here, H corresponds to a maximum range ρ_{\max} , and W corresponds to an azimuth span ϕ . The synchronized data is then processed by a feature extraction network \mathcal{G} , and local features F are aggregated into global descriptors \mathcal{D} using HOLMES.

A. Preprocessing

1) *Dynamic Removal with Ego-velocity Estimation*: Each 4D radar scan at time k , $\mathcal{S}_{4D,k} = \{(x_i, y_i, z_i, v_i^d, \sigma_i)\}_{i=1}^N$, comprises N points with 3D coordinates (x_i, y_i, z_i) , Doppler velocity v_i^d , and RCS σ_i . Our approach employs the 3-Point RANSAC-LSQ [24] to estimate the ego-velocity, filtering out moving objects and mitigating multipath effects. We apply the denoising and refinement function $f_{\text{removal}} : \mathcal{S}_{4D,k} \rightarrow \mathcal{S}'_{4D,k}$,

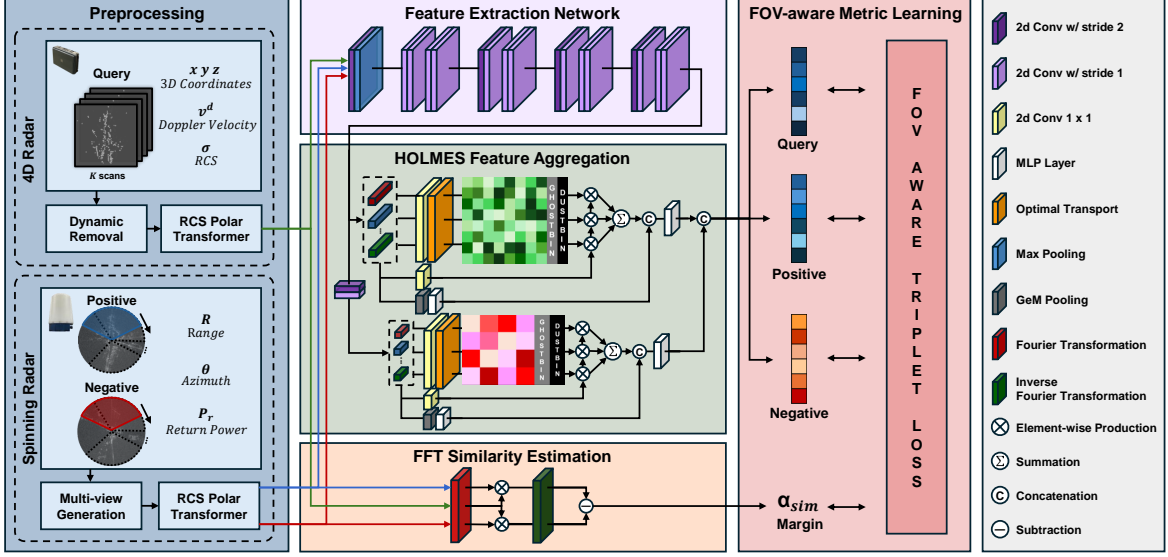


Fig. 2: The overall pipeline of SHeRLoc. RCS polar images I_{4D} and I_{spin} are generated from heterogeneous radars and processed through a shared feature extraction network \mathcal{G} . Local features F are aggregated into global descriptors \mathcal{D} using the HOLMES method.

which removes points with extreme values in $\{z_i, \sigma_i\}$ and eliminates clutter and ground returns. Thus, the resulting refined scan $S'_{4D,k} \in \mathbb{R}^{N^7 \times 5}$ ensures robust localization.

2) *FOV Matching with Multi-view Polar Projection*: Prior works [16, 25] address varying FOV issues in panoramic front-view domains using sliding windows. However, this is unsuitable for spinning radar lacking data along the z -axis. Instead, we adopt a polar BEV projection that ensures a consistent representation across both heterogeneous radars, whereas a Cartesian BEV leaves uncovered regions due to the limited FOV of 4D radar, degrading performance.

For the 4D radar, $S'_{4D,k}$ is projected into RCS polar BEV image $I_{4D,k} \in \mathbb{R}^{H \times W}$ using a polar mapping function $f_{\text{polar}} : S'_{4D,k} \rightarrow I_{4D,k}(r, \theta)$, where r and θ are defined as:

$$r = \left[\sqrt{x^2 + y^2} \right] \frac{H}{\rho_{\max}}, \quad \theta = \left[1 - 2\phi^{-1} \arctan\left(\frac{y}{x}\right) \right] \frac{W}{2}. \quad (1)$$

Each pixel in $I_{4D,k}$ encodes RCS as $2 \cdot \text{rcs} + c$, where c ensures non-negative values, in alignment with the spinning radar, which scales return power in half-dB steps. To form a temporally aggregated, denser 4D radar image $I_{4D,t}$ at time t , we apply max-pooling over K consecutive frames:

$$I_{4D,t}(r, \theta) = \max_{k \in \{t-K+1, \dots, t\}} I_{4D,k}(r, \theta). \quad (2)$$

For the spinning radar, we rescale the scan $S_{\text{spin},t} \in \mathbb{R}^{N_r \times N_a}$ to $S'_{\text{spin},t} \in \mathbb{R}^{H \times 3W}$ and generate multiple polar BEV views using a sliding window of size $H \times W$ along the azimuthal axis. Specifically, we extract n_v views $\{M_{\text{spin},t}^j \in \mathbb{R}^{H \times W}\}_{j=1}^{n_v}$ from $S'_{\text{spin},t}$ at distinct viewpoints, defined as:

$$M_{\text{spin},t}^j = S'_{\text{spin},t}[:, \Delta \cdot (j-1) : \Delta \cdot (j-1) + W], \quad (3)$$

where Δ is the azimuth offset between consecutive views. This multi-view generation function $f_{\text{multiview}} : S'_{\text{spin},t} \rightarrow \{M_{\text{spin},t}^j\}_{j=1}^{n_v}$ ensures 360° FOV coverage, supporting rotation-invariance, detailed in Section III-E.

3) *RCS Matching*: We match RCS values σ with return power P_r using the classical radar equation, formulated as:

$$P_r = \frac{P_t \cdot G^2 \cdot \lambda^2 \cdot \sigma}{(4\pi)^3 \cdot R^4}, \quad (4)$$

where P_t is the transmitted power, G is the antenna gain, λ is the wavelength, and R is the range. An object at height h above the ground and slant range R forms an angle α given by $\sin \alpha = h/R$, or equivalently, $R = h \csc \alpha$. Inspired by air-surveillance radars that maintain constant received power regardless of range [26], modern spinning radars adopt a cosecant-squared beam profile, where the antenna gain satisfies $G \propto R^2$. Assuming constant P_t and λ , the RCS in the radar equation (4) is simplified on the dBsm scale as:

$$\sigma_{\text{dBsm}} = P_r [\text{dB}] + C, \quad (5)$$

where $\sigma_{\text{dBsm}} = 10 \log_{10}(\sigma)$, with the reference RCS defined as $\sigma_{\text{ref}} = 1 \text{ m}^2$, and $C = 40 \log_{10}(R) + 30 \log_{10}(4\pi) - 20 \log_{10}(G \cdot \lambda) - P_t [\text{dB}]$ is a correction constant.

To synchronize $M_{\text{spin},t}$ with $I_{4D,t}$, where pixels represent P_r and σ in half-dB steps, respectively, we precompute a correction term C_{corr} using a small dataset to align $I_{4D,t}$ with the most similar subview $M_{\text{spin},t}^{\max}$. Then, each $M_{\text{spin},t}^j$ is processed by an RCS matching module $f_{\text{rcs}} : M_{\text{spin},t}^j \rightarrow I_{\text{spin},t}^j$ to produce the final RCS polar BEV representation:

$$I_{\text{spin},t}^j = f_{\text{rcs}}(M_{\text{spin},t}^j) = M_{\text{spin},t}^j + C_{\text{corr}}, \quad (6)$$

where C_{corr} is obtained by optimizing a per-frame correction term k_i to minimize the Huber loss. Let the set of valid pixel coordinates be: $\Omega_i = \{(r, \theta) \mid M_{\text{spin},i}^{\max}(r, \theta) \neq 0 \text{ and } I_{4D,i}(r, \theta) \neq 0\}$, and define the Huber loss as:

$$L_\delta(r) = \begin{cases} \frac{1}{2}r^2, & \text{if } |r| \leq \delta, \\ \delta(|r| - \frac{1}{2}\delta), & \text{if } |r| > \delta. \end{cases} \quad (7)$$

Then, The loss for each image pair i can be formulated as:

$$L_i(k_i) = \frac{1}{|\Omega_i|} \sum_{(r, \theta) \in \Omega_i} L_\delta(I_{4D,i}(r, \theta) - (M_{\text{spin},i}^{\max}(r, \theta) + k_i)). \quad (8)$$

To ensure smooth variation of k_i , we introduce a regularization term with factor λ in the joint optimization problem:

$$\{k_i^*\}_{i=1}^N = \underset{\{k_i\}_{i=1}^N}{\text{argmin}} \left(\sum_{i=1}^N L_i(k_i) + \lambda \sum_{j=2}^N (k_j - k_{j-1})^2 \right). \quad (9)$$

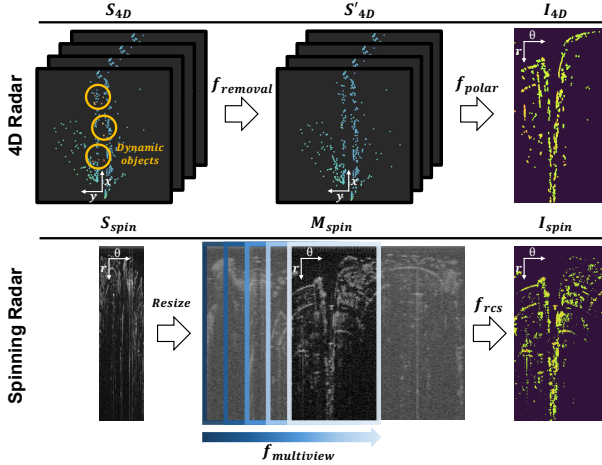


Fig. 3: The pipeline of RCS polar synchronization. The turbo colormap is applied to I_{4D} and I_{spin} for visualization clarity.

Then, we compute $C_{\text{corr}} = \frac{1}{N} \sum_{i=1}^N k_i^*$. As shown in Fig. 3, our preprocessing pipeline filters unreliable data and synchronizes the FOV and data domain between heterogeneous radars to produce a RCS polar BEV representation.

B. Feature Extraction Network

The input to the Feature Extraction Network consists of the synchronized data, I_{4D} and I_{spin} . Traditional heterogeneous place recognition methods require separate encoders for each sensor [18] or a backbone network for independent learning [16, 19]. However, due to the shared synchronized RCS domain and polar BEV format, our approach allows the use of a common network, unlike previous methods. As illustrated in Fig. 2, $I_{4D}, I_{\text{spin}} \in \mathbb{R}^{H \times W}$ are fed into a ResNet-based architecture [27] $\mathcal{G} : I_{4D}, I_{\text{spin}} \rightarrow F_{4D}, F_{\text{spin}}$, generating the feature maps $F_{4D}, F_{\text{spin}} \in \mathbb{R}^{C \times H/32 \times W/32}$.

C. Multi-scale Descriptors with Optimal Transport

To tackle varying density, scanning patterns, and noise-induced uninformative features, we propose a feature aggregation method called HOLMES, Hierarchical Optimal Match Extraction System. We introduce a novel hierarchical framework that combines local RCS patterns and global scene structures. Mid-level features form a local feature matrix $\mathbf{F}_M \in \mathbb{R}^{n_M \times d_f}$, and high-level features, processed through an additional CNN layer, form $\mathbf{F}_H \in \mathbb{R}^{n_H \times d_f}$, where n is the number of spatial locations and d_f is the feature dimension. To leverage the mid-level local features, a convolution layer predicts a score matrix $\mathbf{S} \in \mathbb{R}^{n_M \times m_M}$ for \mathbf{F}_M , where m_M denotes the number of clusters. Inspired by GhostVLAD [30], we extend SALAD's dustbin with a *ghostbin* to handle noise points, resulting in a score matrix

$\bar{\mathbf{S}} \in \mathbb{R}^{n_M \times (m_M + 2)}$. The Sinkhorn algorithm [31] optimizes feature-to-cluster assignments, yielding a refined matrix $\mathbf{R} \in \mathbb{R}^{n_M \times m_M}$ by normalizing $\exp(\bar{\mathbf{S}})$ and dropping dustbin and ghostbin. Unlike SALAD's fixed regularization, we introduce an adaptive entropy regularization based on RCS feature x_i :

$$\text{reg} = 1 + 2 \cdot \tanh \left(\frac{\frac{1}{N} \sum_{i=1}^N (x_i - \mu)^2}{2(\mu + \epsilon)} \right), \quad (10)$$

where μ is the mean and N is the number of elements. In this formulation, high feature variance induces smooth matching for improved stability, while low variance leads to precise matching. Then, the aggregated feature matrix $\mathbf{V} \in \mathbb{R}^{m_M \times l_M}$ with the cluster dimension l_M is computed as:

$$V_{j,k} = \sum_{i=1}^n R_{i,k} \cdot F_{i,j}. \quad (11)$$

Meanwhile, GeM pooling and MLP layers produce a global representation $\mathbf{G} \in \mathbb{R}^{s_M}$. Concatenating \mathbf{V} and \mathbf{G} yields $\mathbf{g} \in \mathbb{R}^{m_M \cdot l_M + s_M}$, which is then transformed by a learnable weight matrix $\mathbf{H} \in \mathbb{R}^{(m_M \cdot l_M + s_M) \times d_M}$ into the mid-level descriptor $\mathcal{D}_M \in \mathbb{R}^{d_M}$. Applying the same process to \mathbf{F}_H produces a high-level descriptor $\mathcal{D}_H \in \mathbb{R}^{d_H}$. By concatenating the mid-level descriptor, the HOLMES \mathcal{H} generates the final multi-scale descriptor $\mathcal{D} = \mathcal{D}_M \oplus \mathcal{D}_H \in \mathbb{R}^{d_M + d_H}$.

D. FOV-aware Metric Learning

1) *FOV-aware Data Mining*: We introduce a FOV-aware data mining approach that selects positive and negative samples based on view similarity. For efficient similarity computation, we leverage the Convolution Theorem, performing computations in the frequency domain [32]. Concretely, the cross-correlation between two scans I_1 and I_2 is defined as:

$$\text{Sim}(I_1, I_2) = \frac{\max \left[\mathcal{F}^{-1} \left(\mathcal{F}(I_1) \cdot \overline{\mathcal{F}(I_2)} \right) \right]}{\|I_1\|_2 \cdot \|I_2\|_2}, \quad (12)$$

where \mathcal{F} and \mathcal{F}^{-1} denote the Fourier and inverse Fourier transforms, respectively. The complexity is reduced from $\mathcal{O}(N^2)$ to $\mathcal{O}(N \log N)$, making data mining time-efficient.

From the multi-view set $\{I_{\text{spin},t}^j\}_{j=1}^{n_v}$, we select the scan $I_{\text{spin},t}^{\max}$ that has the highest similarity to the corresponding $I_{4D,t}$. Then, $I_{\text{spin},t}^{\max}$ with the closest timestamps is labeled as a positive. In contrast, scans beyond the 25 m radius are considered negative, even if their FOV partially overlap, ensuring both spatially and viewpoint-wise meaningful.

2) *FOV-aware Triplet Loss*: To train the network with the mined samples, we adopt a FoV-aware triplet loss formulation. The objective is to bring positive samples closer in the embedding space while pushing negatives apart, with a margin that dynamically adapts to the degree of similarity:

$$\mathcal{L}_{\text{triplet}} = \max \left(d(x_i^q, x_j^p) - \min_{n=1}^N d(x_i^q, x_j^n) + \alpha_{\text{sim}}, 0 \right), \quad (13)$$

where x_i^q is the query pair, x_j^p is the positive pair, x_j^n are negative pair, and $d(\cdot)$ denotes the L_2 distance in the embedding space. The adaptive margin α_{sim} is defined as:

$$\alpha_{\text{sim}} = \gamma (\text{Sim}(\mathbf{q}, \mathbf{p}) - \text{Sim}(\mathbf{q}, \mathbf{n})), \quad (14)$$

where γ is a scale factor. By incorporating similarity into the margin, the loss becomes sensitive to FOV overlap. If a negative has a similar view to the query, the margin becomes smaller, making the model focus on harder negatives.

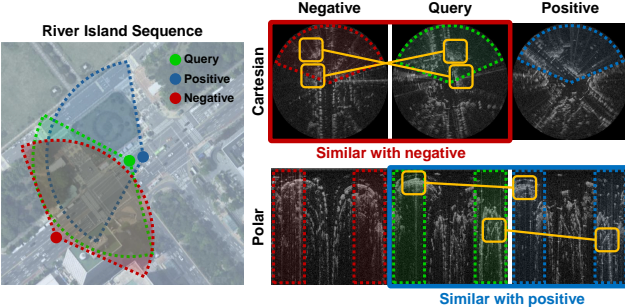


Fig. 4: For a far but overlapping negative and a nearby but rotated positive, Cartesian BEV yields higher similarity with the negative due to rotation variance. In contrast, polar BEV produces higher similarity with the positive, demonstrating robustness to rotation.

E. Rotation Invariance and Intentional Translation Variance

As shown in Fig. 4, negatives that are spatially distant but share an overlapping FOV produce similar features when using Cartesian BEV representations, as seen in [11, 18]. Furthermore, nearby positives may exhibit feature mismatches due to small rotations. These issues are particularly problematic in long-range radar-based PR. To address this, we leverage the polar transform f_{polar} , multi-view generation $f_{\text{multiview}}$, feature extraction \mathcal{G} , and HOLMES \mathcal{H} to achieve rotation invariance and intentional translation variance.

1) *Feature Extraction Equivariance*: Since the transformation $T_{\delta\theta}$ corresponds to a shift in the azimuth dimension and $f_{\text{multiview}}$ operates uniformly across θ , the output of $f_{\text{multiview}}$ is shifted by the same $\delta\theta$: $f_{\text{multiview}}(T_{\delta\theta}S(r, \theta)) = T_{\delta\theta}f_{\text{multiview}}(S(r, \theta))$. Similarly, the CNN-based network \mathcal{G} preserves translation-equivariance up to edge effects [33]. Therefore, both $f_{\text{multiview}}$ and \mathcal{G} maintain the translation-equivariance property. Theoretically, we have to generate infinite multi-views, and aliasing may occur due to downsampling. However, robust performance is achieved with a limited number of multi-views, detailed in Section IV-E.

2) *HOLMES Invariance*: \mathcal{H} processes feature maps F to produce $\mathcal{D}_M \oplus \mathcal{D}_H \in \mathbb{R}^{d_M+d_H}$. GeM Pooling produces a global feature \mathbf{G} , invariant to translations as the summation is order-independent. A convolutional layer produces a score matrix $\mathbf{S} \in \mathbb{R}^{n \times m}$ for Optimal Transport, and the Sinkhorn algorithm computes assignments $\mathbf{R} \in \mathbb{R}^{n \times m}$. The aggregated feature $\mathbf{V}_{j,k} = \sum_{i=1}^n R_{i,k} \cdot F_{i,j}$ is invariant, as summation reorders with translated inputs $F'_j(r, \theta)$. Ghostbin and dustbin discard non-informative points, preserving invariance by excluding spatial dependencies. For multi-scale processing, high-level features \mathbf{F}_H follow the same process, yielding \mathcal{D}_H . Concatenation $(\mathcal{D}_M \oplus \mathcal{D}_H)$ remains invariant to cyclic shifts. For translated feature maps $F'_j(r, \theta)$, \mathcal{H} yields $\mathbf{D}'_M \oplus \mathbf{D}'_H = \mathcal{H}(F'_j(r, \theta)) = \mathcal{H}(F_j(r, \theta)) = \mathcal{D}_M \oplus \mathcal{D}_H$. Thus, our proposed HOLMES network is translation-invariant.

3) *Pipeline Invariance*: A rotated scan $I'(r, \theta) = I(r, \theta + \delta\theta)$ shifts multi-view azimuths cyclically. The feature extraction network outputs $F'_j(r, \theta) = F_j(r, \theta - \theta_0)$, and HOLMES produces an invariant descriptor. With polar BEV ensuring translation variance, the pipeline is rotation-invariant and intentionally translation variant, satisfying $\mathcal{H}(\mathcal{G}(f_{\text{multiview}}(T_{\delta\theta}S(r, \theta))) = \mathcal{H}(\mathcal{G}(f_{\text{multiview}}(S(r, \theta)))$.

IV. EXPERIMENTAL RESULTS

A. Heterogeneous Radar Dataset

To evaluate SHeRLoc, a dataset must include both 4D radar and spinning radar. Existing public datasets, such as Oxford Radar RobotCar [3] and MulRan [4], are limited to spinning radar, while NTU4DRadLM [34] and SNAIL Radar [35] focus solely on 4D radar. In contrast, HeRCULES [36] is the only publicly available heterogeneous range sensor dataset, integrating 4D radar, spinning radar, and FMCW LiDAR, making it uniquely suited for evaluating SHeRLoc. Training was conducted on the Mountain01, Mountain02, Mountain03, Bridge01, Stream02, Parking Lot03, and Parking Lot04 sequences.

B. Implementation Details

We trained SHeRLoc on a GeForce RTX 3090 using the AdamW optimizer with CosineAnnealingLR scheduler, starting with a learning rate of 1e-3 and decaying to a minimum of 1e-5 over 20 epochs. For the polar BEV projection, the resolution of a 150m, 120° polar image is 384x192. The multi-view offset Δ is set to 10°(16 pixels) and λ is set to 0.1 for (9). For HOLMES, (m_M, l_M, s_M, d_M) are set to (64, 256, 256, 256) for the mid-level descriptor, and (m_H, l_H, s_H, d_H) are set to (16, 64, 64, 64) for the high-level descriptor, respectively. We utilize one positive and five negative samples for (13), and the triplet margin loss parameter γ is set to 1.0 for (14). For SHeRLoc-S, a lightweight variant, we utilize a single-scale descriptor of size 256. A retrieval is deemed correct if it is within a 5m radius. The number of scans K is set to 5.

C. Evaluation Metrics

We employed Recall@K (R@K) and Average Recall@K (AR@K) as metrics for evaluation, defined as:

$$R@K = \frac{TP_K}{GT}, \quad AR@K = \frac{1}{S} \sum_{s=1}^S R@K_s, \quad (15)$$

where GT is the number of ground-truth, TP_K denotes the number of true positives found within the top K retrieval candidates, and S is the number of sequences. Also, the Precision-Recall (PR) curve is utilized to assess the overall performance. Precision and recall are defined as:

$$\text{Precision} = \frac{TP}{TP + FP}, \quad \text{Recall} = \frac{TP}{TP + FN}, \quad (16)$$

where TP, FP, and FN are true positive, false positive, and false negative, respectively. The PR curve plots precision vs. recall across a range of thresholds.

D. Comparison with State-of-the-Art Methods

As the first heterogeneous radar PR model, SHeRLoc was compared against homogeneous PR SOTA models, including spinning radar PR methods Radar Scan Context [4], RaPlace [8], RadVLAD, and FFT-RadVLAD [9], as well as SoC radar PR models Autoplace [11], TransLoc4D [14], and the LiDAR PR method MinkLoc3Dv2 [37]. For fair comparison, we used 5-scan aggregation for 4D radar and applied RCS matching for spinning radar across all models.

TABLE I: Performance Comparison for Single-session Place Recognition with Heterogeneous Radar in Various Challenging Conditions (⊗: Clear, ⚡: Dusk, ⚡: Night, ⛃: Cloud, ⛈: Snow, 🚗: dynamic object-rich, **Bold** : Best, Underline : Second Best)

Methods	Sports Complex								Library								River Island							
	01 ⚈		02 ⚡		03 ⚈		01 ⚈		02 ⚡		03 ⚈		01 ⚈ 🚗		02 ⚈ 🚗		03 ⚈ 🚗		01 ⚈ 🚗		02 ⚈ 🚗		03 ⚈ 🚗	
	R@1	R@1%	R@1	R@1%	R@1	R@1%	R@1	R@1%	R@1	R@1%	R@1	R@1%	R@1	R@1%	R@1	R@1%	R@1	R@1%	R@1	R@1%	R@1	R@1%	R@1	R@1%
Radar SC [4]	0.047	0.135	0.042	0.061	0.044	0.064	0.040	0.060	0.041	0.063	0.042	0.066	0.010	0.020	0.004	0.012	0.005	0.030						
RaPlace [8]	0.042	0.148	0.056	0.156	0.025	0.152	0.035	0.069	0.040	0.090	0.016	0.123	0.002	0.152	0.000	0.024	0.004	0.162						
RadVLAD [9]	0.019	0.334	0.051	0.222	0.022	0.426	0.011	0.237	0.014	0.295	0.012	0.245	0.001	0.217	0.066	0.543	0.006	0.367						
FFT-RadVLAD [9]	0.040	0.344	0.014	0.186	0.022	0.377	0.023	0.287	0.014	0.273	0.011	0.229	0.002	0.330	0.026	0.533	0.001	0.488						
Autoplace [11]	0.015	0.198	0.046	0.098	0.017	0.186	0.010	0.129	0.031	0.131	0.018	0.122	0.003	0.051	0.001	0.009	0.001	0.021						
SHeRLoc-S	0.857	0.924	0.975	0.985	0.945	0.981	0.866	0.917	0.925	0.950	0.850	0.891	0.899	0.965	0.868	0.963	0.850	0.945						
SHeRLoc	0.900	0.936	0.962	0.987	0.958	0.980	0.881	0.936	0.938	0.964	0.868	0.912	0.880	0.957	0.860	0.952	0.858	0.959						

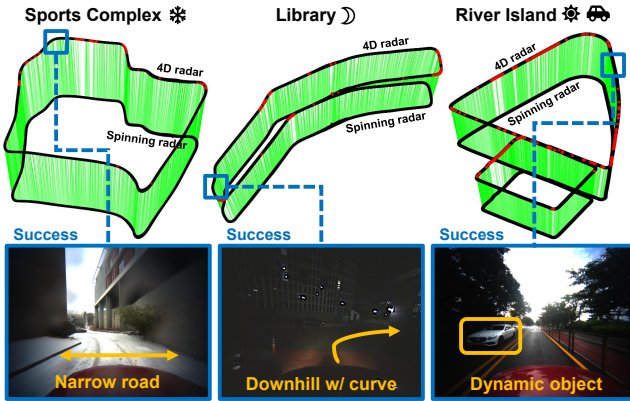


Fig. 5: Trajectory from Sports Complex, Library, and River Island sequences, with green indicating true matching pairs, highlighting SHeRLoc’s robustness in challenging scenarios.

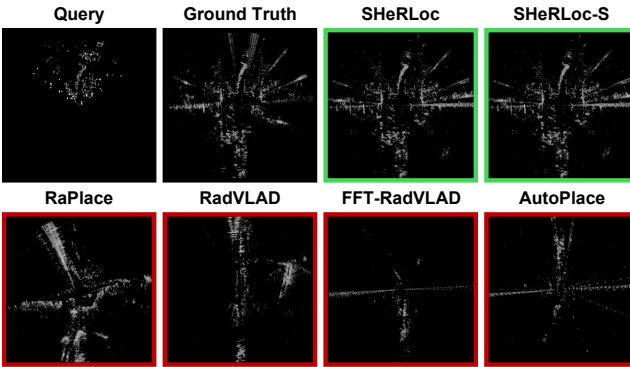


Fig. 6: Qualitative results of SOTA methods on a challenging query. Green indicates successful retrieval, and red indicates failure.

1) *Heterogeneous Radar Single-session PR*: For single-session evaluation, spinning radar data were used as the database, and 4D radar data were used as queries for all the Sports Complex, Library, and River Island sequences. As shown in Table I, SHeRLoc outperforms others across all sequences. Furthermore, the faster and more lightweight SHeRLoc-S also surpasses all SOTA methods. As illustrated in Fig. 5, SHeRLoc successfully matches nearly every query, even in challenging scenarios. Evaluations on diverse sequences from the HeRCULES dataset demonstrate that SHeRLoc achieves robust PR not only in daytime conditions but also in challenging environments such as night, snow, cloud, and dynamic object-rich settings.

2) *Heterogeneous Radar Multi-session PR*: For multi-session evaluation, spinning radar data from sequence 01 were used as the database, and 4D radar from sequences 02 and 03 were used as queries. Quantitative results are presented in Table II, with qualitative analysis shown in Fig. 6

TABLE II: Performance Comparison for Multi-session Place Recognition with Heterogeneous Radar and Homogeneous Radar

Methods	Sports Complex				Library				AR@1	
	01 - 02		01 - 03		01 - 02		01 - 03			
	R@1	R@1%	R@1	R@1%	R@1	R@1%	R@1	R@1%		
RaPlace [8]	0.024	0.056	0.016	0.057	0.021	0.044	0.011	0.023	0.018	
RadVLAD [9]	0.011	0.118	0.005	0.214	0.012	0.138	0.011	0.073	0.010	
FFT-RadVLAD [9]	0.006	0.121	0.007	0.182	0.015	0.217	0.016	0.136	0.011	
Autoplace [11]	0.007	0.071	0.012	0.070	0.022	0.129	0.007	0.119	0.012	
SHeRLoc-S	0.796	0.890	0.580	0.696	0.822	0.892	0.618	0.757	0.704	
SHeRLoc	0.812	0.893	0.650	0.759	0.817	0.887	0.610	0.743	0.722	
Autoplace [11]	0.799	0.967	0.725	0.945	0.812	0.986	0.619	0.901	0.738	
MinkLoc3Dv2 [37]	0.837	0.982	0.743	0.977	0.725	0.981	0.619	0.963	0.735	
TransLoc4D [14]	0.833	0.970	0.804	0.976	0.801	0.991	0.676	0.940	0.779	
SHeRLoc-S	0.866	0.945	0.803	0.925	0.914	0.986	0.908	0.988	0.873	
SHeRLoc	0.904	0.961	0.843	0.949	0.950	0.995	0.923	0.988	0.905	
RaPlace [8]	0.943	0.962	0.927	0.989	0.998	1.000	0.906	0.955	0.944	
RadVLAD [9]	0.996	1.000	0.981	1.000	0.999	1.000	0.975	1.000	0.988	
FFT-RadVLAD [9]	0.996	1.000	0.985	1.000	0.999	1.000	0.979	1.000	0.990	
SHeRLoc-S	0.963	0.993	1.000	0.981	0.999	0.999	1.000	0.936	0.997	0.965
SHeRLoc	0.993	1.000	0.981	0.999	0.999	1.000	0.998	1.000	0.993	

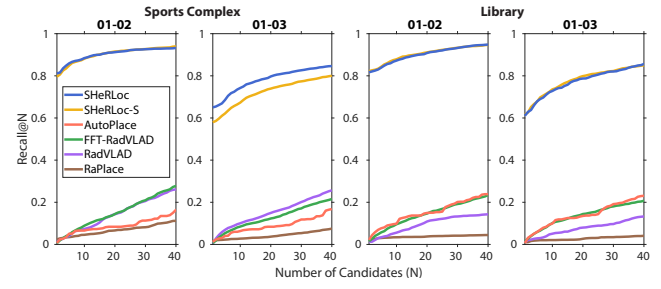


Fig. 7: R@N curves for multi-session PR with heterogeneous radar. SHeRLoc outperforms all methods when retrieving 40 candidates.

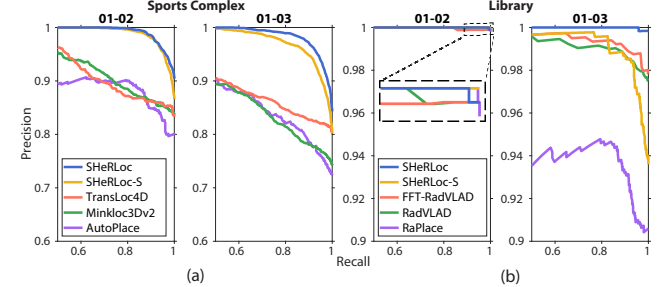


Fig. 8: Precision-Recall curve for homogeneous radar multi-session PR: (a) 4D radar-based PR results on the Sports Complex, (b) Spinning radar-based PR results on the Library.

and recall@N curves depicted in Fig. 7. Unlike most other models, which exhibit significant performance degradation due to environmental changes over time, SHeRLoc demonstrates robust PR across multiple sessions.

3) *Homogeneous Radar Multi-session PR*: SHeRLoc was compared with Autoplace [11], MinkLoc3Dv2 [37], and TransLoc4D [14] for 4D radar PR, and with RaPlace [8], RadVLAD, and FFT-RadVLAD [9] for spinning radar PR. The results are reported in Table II and Fig. 8, confirming SHeRLoc’s superior performance despite not being designed for homogeneous radar. For 4D radar PR, it demonstrates top

TABLE III: Performance Comparison under Random Rotation

Methods	Sports Complex		Library		River Island	
	AR@1	AR@1%	AR@1	AR@1%	AR@1	AR@1%
Radar SC [4]	0.045	0.087	0.041	0.063	0.007	0.021
RaPlace [8]	0.030	0.204	0.130	0.229	0.002	0.191
RadVLAD [9]	0.011	0.318	0.012	0.249	0.016	0.402
FFT-RadVLAD [9]	0.019	0.310	0.012	0.234	0.019	0.429
Autoplace [11]	0.026	0.161	0.020	0.127	0.001	0.122
SHeRLoc-S	0.905	0.959	0.828	0.893	0.710	0.880
SHeRLoc	0.918	0.964	0.858	0.920	0.733	0.904

TABLE IV: Performance Comparison for Place Recognition with Spinning Radar as Database and FMCW LiDAR as Query

Methods	Sports Complex		Library		River Island	
	AR@1	AR@1%	AR@1	AR@1%	AR@1	AR@1%
Radar SC [4]	0.141	0.188	0.046	0.060	0.033	0.050
Autoplace [11]	0.017	0.105	0.014	0.059	0.004	0.041
Radar-to-LiDAR [17]	0.656	0.832	0.468	0.769	0.229	0.530
SHeRLoc-S	0.948	0.971	0.895	0.945	0.932	0.983
SHeRLoc	0.948	0.977	0.899	0.931	0.952	0.987

performance across nearly all sequences. For spinning radar PR, SHeRLoc achieves an AR@1 of 0.993, surpassing all SOTA methods. Furthermore, PR curves indicate that SHeRLoc achieves high precision and recall for both radar types under diverse conditions, demonstrating robust performance for both homogeneous and heterogeneous radar.

E. Robustness against Random Rotation

In real-world scenarios, random yaw angle rotations between the database and query are common, making rotation robustness crucial. Therefore, we conducted experiments with random yaw angle rotations on database scans within a 360° range. Through polar domain multi-view generation and the rotation-invariant design of the HOLMES feature aggregation network, SHeRLoc demonstrates superior rotation robustness compared to other methods. As shown in Table III, comparing AR@1 with SOTA methods on Sports Complex, Library, and River Island, both SHeRLoc and SHeRLoc-S consistently achieve the best performance. This robust performance, despite angle variations, demonstrates that a limited number of multi-views is sufficient for achieving robust rotation invariance.

F. Heterogeneous Range Sensor Place Recognition

We evaluated SHeRLoc's generalization performance using FMCW LiDAR queries and a spinning radar database, comparing it with Radar Scan Context [4], Autoplace [11], and Radar-to-LiDAR [17]. For heterogeneous range sensor PR, we utilized radial velocity in a manner analogous to 4D radar, and replaced radar RCS with LiDAR reflectivity ρ , which satisfies the following classical LiDAR equation:

$$I \propto \frac{P_t D_r^2 \eta^2 \rho \cos \alpha_i}{4R^2}, \quad (17)$$

where I is the LiDAR intensity, P_t is the transmitted power, D_r is the receiver aperture diameter, η is the system transmission factor, α_i is the angle of incidence, and R is the range. Through our preprocessing, the data distributions of FMCW LiDAR and spinning radar become highly similar, as shown in Fig. 9. Additionally, Table IV shows that SHeRLoc performs robustly even across heterogeneous range sensors.

TABLE V: Ablation Study on SHeRLoc Components to Evaluate Individual Contributions

S	P	R	A	Sports Complex				Library			
				01 - 02		01 - 03		01 - 02		01 - 03	
				R@1	R@1%	R@1	R@1%	R@1	R@1%	R@1	R@1%
✗	✗	✗	✗	0.009	0.015	0.009	0.013	0.019	0.032	0.016	0.035
✓	✗	✗	✗	0.013	0.072	0.009	0.032	0.011	0.022	0.008	0.031
✓	✓	✗	✗	0.659	0.792	0.516	0.633	0.657	0.749	0.497	0.665
✓	✓	✓	✗	0.737	0.840	0.529	0.625	0.751	0.836	0.514	0.679
✓	✓	✓	✓	0.812	0.893	0.650	0.759	0.817	0.887	0.610	0.743

TABLE VI: Ablation Study on Feature Aggregation Method

Methods	Size	Sports Complex				Library			
		01 - 02		01 - 03		01 - 02		01 - 03	
		R@1	R@1%	R@1	R@1%	R@1	R@1%	R@1	R@1%
NetVLAD [1]	32768	0.378	0.598	0.151	0.254	0.302	0.474	0.102	0.218
MAC [38]	512	0.700	0.846	0.404	0.534	0.525	0.657	0.258	0.514
SPoC [39]	512	0.282	0.517	0.112	0.210	0.155	0.258	0.036	0.150
GeM [29]	512	0.486	0.717	0.234	0.384	0.324	0.475	0.091	0.197
SALAD [28]	8448	0.371	0.611	0.170	0.295	0.330	0.497	0.094	0.235
HOLMES-S*	256	0.769	0.882	0.616	0.730	0.840	0.909	0.587	0.756
HOLMES-S	256	0.796	0.890	0.580	0.696	0.822	0.892	0.618	0.757
HOLMES	320	0.812	0.893	0.650	0.759	0.817	0.887	0.610	0.743

HOLMES-S*: HOLMES-S without ghostbin and adaptive entropy regularization.

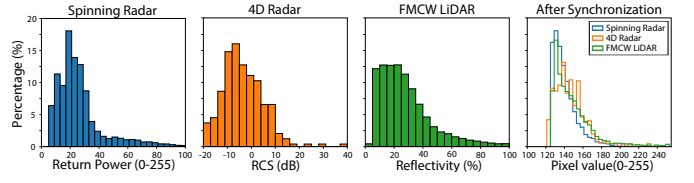


Fig. 9: Data distribution of each sensor and the synchronized data distribution after SHeRLoc's RCS polar domain matching.

G. Ablation Study

1) *SPRA Components*: We compared SHeRLoc variants that progressively incorporate the following modules: **S** (Scan aggregation), **P** (Polar projection), **R** (RCS matching), **A** (Adaptive margin loss). The results in Table V demonstrate how each component contributes to the performance. In the Cartesian domain, performance is significantly poor, and applying **S** alone fails to yield significant improvement. However, combining **S** with **P**, as in our approach, provides an average improvement of 57.2% in recall@1, with **R** further enhancing performance by 5.05%. As illustrated in Fig. 9, while each sensor's raw data has different distributions, our approach using **S**, **P**, and **R** leads to very similar data distributions. Finally, **A** contributes an additional 8.95% increase, resulting in an overall improvement of approximately 71.2%.

2) *Feature Aggregation*: We evaluated the HOLMES feature aggregation against existing methods, including NetVLAD [1], MAC [38], SPoC [39], GeM [29], and SALAD [28]. As shown in Table VI, widely used methods like GeM pooling are vulnerable to noisy and sparse radar data. Additionally, NetVLAD and SALAD require large descriptor sizes, leading to longer processing times and higher storage demands. In contrast, HOLMES-S, with a compact 256-dimensional descriptor, achieves accurate PR performance through its radar-specific feature aggregation design, including ghostbin and adaptive entropy regularization. Moreover, HOLMES, with a descriptor size of $256 + 64 = 320$ dimensions, further improves performance by employing multi-scale descriptors. As a result, HOLMES outperforms other methods, while requiring less storage and generating each multi-scale descriptor in just 13ms.

V. CONCLUSION

In this work, we introduce SHeRLoc, the first deep network for heterogeneous radar PR. SHeRLoc employs a novel preprocessing method to transform radar data into synchronized RCS polar BEV representations and hierarchical optimal transport-based multi-scale descriptors. Our FOV-aware data mining and adaptive margin-based triplet loss facilitate spatially and viewpoint-wise meaningful metric learning. Evaluations on diverse sequences demonstrate that SHeRLoc achieves robust performance in challenging environments and is applicable to both heterogeneous and homogeneous radar systems, as well as heterogeneous range sensor systems. As the first study on heterogeneous radar PR, SHeRLoc opens new opportunities for cross-modal place recognition, enabling efficient localization of vehicles with automotive 4D radars on pre-built spinning radar maps.

REFERENCES

- [1] R. Arandjelovic, P. Gronat, A. Torii, T. Pajdla, and J. Sivic, “Netvlad: Cnn architecture for weakly supervised place recognition,” in *Proc. IEEE Conf. on Comput. Vision and Pattern Recog.*, 2016, pp. 5297–5307.
- [2] G. Kim and A. Kim, “Scan context: Egocentric spatial descriptor for place recognition within 3d point cloud map,” in *Proc. IEEE/RSJ Int'l. Conf. on Intell. Robots and Sys.*, 2018.
- [3] D. Barnes, M. Gadd, P. Murcutt, P. Newman, and I. Posner, “The oxford radar robotcar dataset: A radar extension to the oxford robotcar dataset,” in *Proc. IEEE Int'l. Conf. on Robot. and Automat.*, 2020, pp. 6433–6438.
- [4] G. Kim, Y. S. Park, Y. Cho, J. Jeong, and A. Kim, “Mulran: Multimodal range dataset for urban place recognition,” in *Proc. IEEE Int'l. Conf. on Robot. and Automat.*, 2020, pp. 6246–6253.
- [5] D. Barnes and I. Posner, “Under the radar: Learning to predict robust keypoints for odometry estimation and metric localisation in radar,” in *Proc. IEEE Int'l. Conf. on Robot. and Automat.*, 2020, pp. 9484–9490.
- [6] Š. Săftescu, M. Gadd, D. De Martini, D. Barnes, and P. Newman, “Kidnapped radar: Topological radar localisation using rotationally-invariant metric learning,” in *Proc. IEEE Int'l. Conf. on Robot. and Automat.*, 2020, pp. 4358–4364.
- [7] M. Gadd, D. De Martini, and P. Newman, “Look around you: Sequence-based radar place recognition with learned rotational invariance,” in *2020 IEEE/ION Position, Location and Navigation Symposium*. IEEE, 2020, pp. 270–276.
- [8] H. Jang, M. Jung, and A. Kim, “Raplace: Place recognition for imaging radar using radon transform and mutable threshold,” in *Proc. IEEE/RSJ Int'l. Conf. on Intell. Robots and Sys.*, 2023.
- [9] M. Gadd and P. Newman, “Open-radvlad: Fast and robust radar place recognition,” in *2024 IEEE Radar Conference*, 2024, pp. 1–6.
- [10] H. Kim, B. Choi, E. Choi, and Y. Cho, “Referee: Radar-based lightweight and robust localization using feature and free space,” *IEEE Robot. and Automat. Lett.*, 2024.
- [11] K. Cai, B. Wang, and C. X. Lu, “Autoplace: Robust place recognition with single-chip automotive radar,” in *Proc. IEEE Int'l. Conf. on Robot. and Automat.*, 2022, pp. 2222–2228.
- [12] C. Meng, Y. Duan, C. He, D. Wang, X. Fan, and Y. Zhang, “mmplace: Robust place recognition with intermediate frequency signal of low-cost single-chip millimeter wave radar,” *IEEE Robot. and Automat. Lett.*, 2024.
- [13] D. C. Herraez, L. Chang, M. Zeller, L. Wiesmann, J. Behley, M. Heidingsfeld, and C. Stachniss, “Spr: Single-scan radar place recognition,” *IEEE Robot. and Automat. Lett.*, 2024.
- [14] G. Peng, H. Li, Y. Zhao, J. Zhang, Z. Wu, P. Zheng, and D. Wang, “Transloc4d: Transformer-based 4d radar place recognition,” in *Proc. IEEE Conf. on Comput. Vision and Pattern Recog.*, 2024, pp. 17595–17605.
- [15] M. Hilger, V. Kubelka, D. Adolfsson, R. Becker, H. Andreasson, and A. J. Lilienthal, “Introspective loop closure for slam with 4d imaging radar,” *arXiv preprint arXiv:2503.02383*, 2025.
- [16] G. Yao, X. Li, L. Fu, and Y. Pan, “Monocular visual place recognition in lidar maps via cross-modal state space model and multi-view matching,” *arXiv preprint arXiv:2410.06285*, 2024.
- [17] H. Yin, X. Xu, Y. Wang, and R. Xiong, “Radar-to-lidar: Heterogeneous place recognition via joint learning,” *Frontiers in Robotics and AI*, vol. 8, p. 661199, 2021.
- [18] A. Nayak, D. Cattaneo, and A. Valada, “Ralf: Flow-based global and metric radar localization in lidar maps,” in *Proc. IEEE Int'l. Conf. on Robot. and Automat.*, 2024, pp. 5097–5103.
- [19] D. Cattaneo, M. Vaghi, S. Fontana, A. L. Ballardini, and D. G. Sorrenti, “Global visual localization in lidar-maps through shared 2d-3d embedding space,” in *2020 IEEE International Conference on Robotics and Automation*. IEEE, 2020, pp. 4365–4371.
- [20] W. Xie *et al.*, “Modalink: Unifying modalities for efficient image-to-pointcloud place recognition,” in *Proc. IEEE/RSJ Int'l. Conf. on Intell. Robots and Sys.*, 2024, pp. 3326–3333.
- [21] Z. Zhou, J. Xu, G. Xiong, and J. Ma, “Lcpr: A multi-scale attention-based lidar-camera fusion network for place recognition,” *IEEE Robotics and Automation Letters*, vol. 9, no. 2, pp. 1342–1349, 2023.
- [22] S. Fu, Y. Duan, Y. Li, C. Meng, Y. Wang, J. Ji, and Y. Zhang, “Crplace: Camera-radar fusion with bev representation for place recognition,” *arXiv preprint arXiv:2403.15183*, 2024.
- [23] M. Jung, S. Jung, H. Gil, and A. Kim, “Helios: Heterogeneous lidar place recognition via overlap-based learning and local spherical transformer,” *arXiv preprint arXiv:2501.18943*, 2025.
- [24] C. Doer and G. F. Trommer, “An ekf based approach to radar inertial odometry,” in *2020 IEEE International Conference on Multisensor Fusion and Integration for Intelligent Systems*. IEEE, 2020, pp. 152–159.
- [25] Z. Shi, H. Shi, K. Yang, Z. Yin, Y. Lin, and K. Wang, “Panovpr: towards unified perspective-to-equirectangular visual place recognition via sliding windows across the panoramic view,” in *Proc. IEEE Int'l. Transport. Sys. Conf.*, 2023, pp. 1333–1340.
- [26] Z.-C. Hao and M. He, “Developing millimeter-wave planar antenna with a cosecant squared pattern,” *IEEE Trans. Antennas and Prop.*, vol. 65, no. 10, pp. 5565–5570, 2017.
- [27] K. He, X. Zhang, S. Ren, and J. Sun, “Deep residual learning for image recognition,” in *Proc. IEEE Conf. on Comput. Vision and Pattern Recog.*, 2016, pp. 770–778.
- [28] S. Izquierdo and J. Civera, “Optimal transport aggregation for visual place recognition,” in *Proc. IEEE Conf. on Comput. Vision and Pattern Recog.*, 2024, pp. 17658–17668.
- [29] F. Radenović, G. Tolias, and O. Chum, “Fine-tuning cnn image retrieval with no human annotation,” *IEEE Trans. Pattern Analysis and Machine Intell.*, vol. 41, no. 7, pp. 1655–1668, 2018.
- [30] Y. Zhong, R. Arandjelović, and A. Zisserman, “Ghostvlad for set-based face recognition,” in *Computer Vision-ACCV 2018: 14th Asian Conference on Computer Vision, Perth, Australia, December 2–6, 2018, Revised Selected Papers, Part II 14*. Springer, 2019, pp. 35–50.
- [31] M. Cuturi, “Sinkhorn distances: Lightspeed computation of optimal transport,” *Advances in Neural Information Processing Sys. Conf.*, vol. 26, 2013.
- [32] P. Duhamel and M. Vetterli, “Fast fourier transforms: a tutorial review and a state of the art,” *Signal processing*, vol. 19, no. 4, pp. 259–299, 1990.
- [33] T. Cohen and M. Welling, “Group equivariant convolutional networks,” in *International conference on machine learning*. PMLR, 2016, pp. 2990–2999.
- [34] J. Zhang *et al.*, “Ntu4dradlm: 4d radar-centric multi-modal dataset for localization and mapping,” in *Proc. IEEE Int'l. Transport. Sys. Conf.*, 2023, pp. 4291–4296.
- [35] J. Huai, B. Wang, Y. Zhuang, Y. Chen, Q. Li, and Y. Han, “Snail radar: A large-scale diverse benchmark for evaluating 4d-radar-based slam,” *The International Journal of Robotics Research*, p. 02783649251329048, 2024.
- [36] H. Kim *et al.*, “Hercules: Heterogeneous radar dataset in complex urban environment for multi-session radar slam,” in *Proc. of the IEEE International Conference on Robotics and Automation*, 2025.
- [37] J. Komorowski, “Improving point cloud based place recognition with ranking-based loss and large batch training,” in *2022 26th international conference on pattern recognition*. IEEE, 2022, pp. 3699–3705.
- [38] G. Tolias, R. Sicre, and H. Jégou, “Particular object retrieval with integral max-pooling of cnn activations,” *arXiv preprint arXiv:1511.05879*, 2015.
- [39] A. Babenko and V. Lempitsky, “Aggregating deep convolutional features for image retrieval,” *arXiv preprint arXiv:1510.07493*, 2015.